

1 Neutron-Neutron Correlations in the Photofission of U-238

2 J. Burggraf, D.S. Dale, and T. Forest
3

4 *Department of Physics,*
5 *Idaho State University, Pocatello, ID 83201*

6 G. Warren, S. Stave, S. Behling, and E. Church
7

8 *Pacific Northwest National Laboratory, PO Box 999, Richland, Washington 99352*

(Dated: July 2, 2019)

9 **Background:** In the fission of actinides, the nearly back-to-back motion of the fission fragments has a strong
10 effect on the kinematics of fission neutrons. This leads to a favoring of opening angles near 0° and 180° in the
11 neutron-neutron (n-n) opening angle distributions of correlated neutron pairs from the same fission event.

12 **Purpose:** To measure the n-n opening angle and energy correlations in the photofission of ^{238}U . As of this
13 writing, measurements of correlated n-n opening angle distributions have been reported only for the spontaneous
14 and neutron-induced fission of actinides. This work is the first to report such a measurement using photofission
15 and will provide useful experimental input for photofission models used in codes such as MCNP and FREYA.

16 **Method:** Fission is induced using bremsstrahlung photons produced via a low duty factor, pulsed, linear electron
17 accelerator. The bremsstrahlung photon beam impinges upon a ^{238}U target that is surrounded by a large neutron
18 scintillation detection system capable of measuring particle position and time of flight, from which n-n opening
19 angle and energy are measured. Neutron-neutron angular correlations are determined by taking the ratio between
20 a correlated neutron distribution and an uncorrelated neutron distribution formed by the pairing of neutrons pro-
21 duced during different beam pulses. This analysis technique greatly diminishes effects due to detector efficiencies,
22 acceptance, and experimental drifts.

23 **Results:** The angular correlation of neutrons from the photofission of ^{238}U shows a high dependence on neutron
24 energy as well as a dependence on the angle of the emitted neutrons with respect to the incoming photon beam.
25 Angular correlations were also measured using neutrons from the spontaneous fission of ^{252}Cf , showing good
26 agreement with past measurements.

27 **Conclusions:** The measured angular correlations reflect the underlying back-to-back nature of the fission frag-
28 ments. An anomalous decline in n-n yield was observed for opening angles near 180° for ^{238}U .

29 CONTENTS

30 I. Overview of Neutron-Neutron Angular
31 Correlations in Fission
32 A. Theoretical Basis
33 B. Past Measurements: Spontaneous and
34 Neutron Induced Fission
35 C. Considerations for Photofission

36 II. Experimental Setup
37 A. Detectors
38 B. Detector Shielding
39 C. Bremsstrahlung Photon Beam
40 D. DU Target
41 E. Electronics

42 III. Measurement Techniques
43 A. Particle Time of Flight and Energy
44 Determination
45 B. Particle Position Reconstruction
46 C. Measurements with ^{252}Cf

47 IV. Analysis
48 A. Cancelation of Detector Efficiencies, Drifts,
49 and Geometric Phase Space
50 B. Subtraction of Accidental Coincidences

51 V. Potential sources of error

52 A. Correlated versus uncorrelated n-n energy
53 distribution
54 B. Detector Cross-talk
55 1. Simulation of Detector Cross-talk
56 C. Neutron Scattering within the Target

57 VI. Results

58 A. n-n angular correlation versus neutron
59 energy
60 B. Considering θ_{abs}

61 VII. Concluding Remarks

62 VIII. Acknowledgments

63 References

64 I. OVERVIEW OF NEUTRON-NEUTRON 65 ANGULAR CORRELATIONS IN FISSION

66 The fission process is characterized by the emission of
67 neutrons. Neutron emission in fission can be classified
68 into two categories depending on the time of emission:
69 delayed and prompt. Prompt fission neutrons are de-
70 fined as neutrons that are emitted either immediately

71 after ($< 10^{-14}$ seconds) fission, or during the scission
 72 of the nucleus, and account for $\sim 99\%$ of neutron emis-
 73 sion [1]. Delayed neutrons are not relevant to the present
 74 work because they account for only $\sim 1\%$ of total neutron
 75 emission in actinide photofission [1], and they are emit-
 76 ted milliseconds to minutes after fission which is well out-
 77 side the neutron acceptance timing window of the present
 78 work.

79 Prompt fission neutron production occurs by means of
 80 two distinct mechanisms. The dominant mechanism is
 81 neutron emission from the fully accelerated fragments.
 82 The second mechanism, referred to as *early* or *scission*
 83 neutron emission, is the emission of neutrons during ei-
 84 ther the scission of the nucleus or the acceleration of the
 85 fission fragments. A large number of past studies have
 86 established that the majority of prompt fission neutrons
 87 (80%–98%) are emitted from the fully accelerated frag-
 88 ments, while scission neutrons account for the remaining
 89 2%–20% percent [2]. The nature of scission neutrons has
 90 remained elusive since their first tentative observation in
 91 1962 by Bowman *et al.* [3].

92 A. Theoretical Basis

93 The neutron-neutron (n-n) opening angle distribution
 94 of correlated neutron pairs, as seen in the lab frame, is
 95 widely used for the quantification of n-n angular corre-
 96 lations. Angular correlations in fission neutrons arise due
 97 to the kinematics of the fission fragments. It has been
 98 shown that neutrons released from the fully accelerated
 99 fission fragments are evaporated isotropically in the frag-
 100 ment’s rest frame, and are emitted at speeds compara-
 101 ble to that of the fragments themselves [4]. This leads
 102 to the well-known U-shaped distribution in neutron-
 103 neutron opening angle (θ_{nn}), which has been reported
 104 in studies of neutron-induced, spontaneous, and in this
 105 work, photofission. An example of a typical θ_{nn} distri-
 106 bution is seen in Fig. 1.

107 The U-shaped distribution of θ_{nn} can be understood
 108 as the result of the boost provided to the neutrons by the
 109 fission fragments in binary fission. Due to the conserva-
 110 tion of momentum, the fully accelerated fission fragments
 111 are traveling nearly back-to-back, and neutrons emitted
 112 from different fragments are boosted in opposite direc-
 113 tions, whereas neutrons emitted from the same fragment
 114 are boosted in the same direction. Thus, because the
 115 velocities of the fission fragments are large enough to ac-
 116 count for a significant portion of the kinetic energy of
 117 fission neutrons, neutron pairs emitted from the acceler-
 118 ated fragments exhibit a favoring of opening angles near
 119 0° if emitted from the same fragment and 180° if emitted
 120 from different fragments, and consequently, a suppression
 121 of opening angles near 90°.

122 The favoring of large and small n-n opening angles
 123 shows a strong dependence on neutron energy. Neutrons
 124 with higher energy are more likely to have been emitted
 125 along the same direction as the fission fragments and are

126 therefore expected to favor large and small opening an-
 127 gles. The θ_{nn} distribution and its dependence on neutron
 128 energy are expected to shed light on several fundamental
 129 aspects of the fission process including the neutron mul-
 130 tiplicity distributions associated with the light and heavy
 131 fission fragments, the nuclear temperatures of the fission
 132 fragments, and the mass distribution of the fission frag-
 133 ments as a function of energy released. In addition, the
 134 unique kinematics of fission and the resulting n-n corre-
 135 lations have the potential to be the basis for a new tool
 136 to characterize fissionable materials [5].

137 B. Past Measurements: Spontaneous and Neutron 138 Induced Fission

139 The first measurement of the angular correlation
 140 among coincident neutrons from fission was performed
 141 by Debenedetti *et al.* [6] in 1948 from neutron induced
 142 fission of ^{235}U . The next measurement of this type was
 143 performed by Pringle and Brooks in 1975 [7], in which
 144 neutrons emitted from the spontaneous fission (SF) of
 145 ^{252}Cf were found to have high coincidence rates at small
 146 opening angles near 0° and large opening angles near
 147 180°. In order to produce a result that is insensitive
 148 to the effects of detector geometry and efficiency, the
 149 present work uses techniques similar to those used in ref-
 150 erence [7], in which a ratio is taken between a correlated
 151 opening angle distribution and an uncorrelated opening
 152 angle distribution.

153 To date, numerous measurements of n-n angular cor-
 154 relation using ^{252}Cf have been performed [7–10]. This
 155 makes ^{252}Cf a good benchmark for n-n angular corre-
 156 lation measurements. Figure 1 compares measurements
 157 in this work to past measurements of n-n correlations in
 158 the SF of ^{252}Cf . Correlated n-n measurements have also
 159 been performed using thermal induced fission of ^{235}U ,
 160 ^{233}U , and ^{239}Pu [11].

162 C. Considerations for Photofission

163 The photofission reaction occurs during the de-
 164 excitation of a nucleus after the absorption of a pho-
 165 ton. For photon energies between 6 and 25 MeV, this ab-
 166 sorption occurs primarily via the giant dipole resonance
 167 (GDR). One distinct and useful aspect of photofission,
 168 relative to neutron-induced fission, is the low transfer of
 169 angular momentum to the nucleus, which gives rise to a
 170 simpler set of selection rules for the transfer of angular
 171 momentum. For the photofission of even-even nuclei, ex-
 172 citation occurs primarily via electric dipole transitions,
 173 and to a lesser extent electric quadrupole transitions,
 174 which gives rise to anisotropies in the fission fragment
 175 angular distribution that are far more pronounced than
 176 for other types of fission [13]. These anisotropies are ex-
 177 pressed in the angular distribution of emitted neutrons.
 178 For these reasons, photofission is increasingly being used

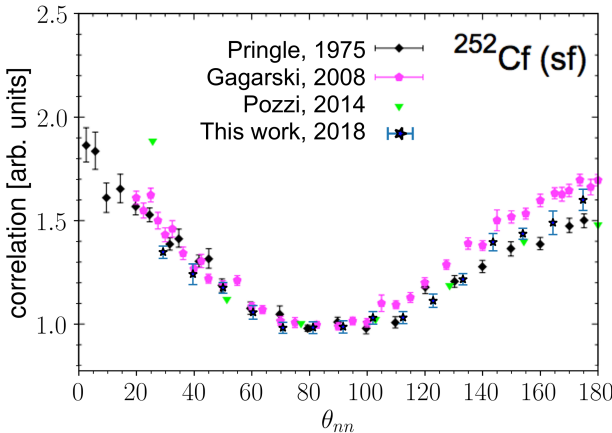


FIG. 1: θ_{nn} distribution from the spontaneous fission of ^{252}Cf . The neutron detection threshold for Pringle [7], Gagarski [10], and Pozzi [12] is 0.425 MeV, 0.425 MeV, and 0.7 MeV, respectively, and for this work is 0.5 MeV.

as a means to study sub-nuclear structures and the fundamentals of the fission process. Such studies are needed in order to dial in various model parameters required for an accurate theoretical description of the fission process.

II. EXPERIMENTAL SETUP

This experiment was carried out at the Idaho Accelerator Center (IAC), using their short-pulsed linear accelerator, which is an L-band frequency (1300 MHz) electron linear accelerator. See section II C for the accelerator parameters used during the experiment. Figure 2 shows a top-down diagram of the experimental arrangement.

A. Detectors

The detection system measures neutron position and time of flight (ToF), which is defined as the time taken for a particle to travel from the fission target to a detector. The purpose of the ToF measurement is to determine the kinetic energy of detected neutrons and to distinguish between photons and neutrons. The detection system's positional precision is ± 9 cm, which gives an average angular precision of $\pm 6^\circ$ in opening angle reconstruction.

The detection system consists of fourteen shielded scintillators made from Polyvinyl Toluene (PVT) arranged in a ring around the target (see Figs. 2 and 3). Attached to both ends of each scintillator are 10-cm long, non-scintillating, ultra-violet transmitting, plastic light-guides. A Hamamatsu 580-17 photomultiplier (PMT) tube is fixed to each light-guide using optical glue. In order to increase the chance that scintillation light remains inside the scintillator, the scintillators were polished to remove micro-imperfections and were then wrapped in reflective aluminized mylar.

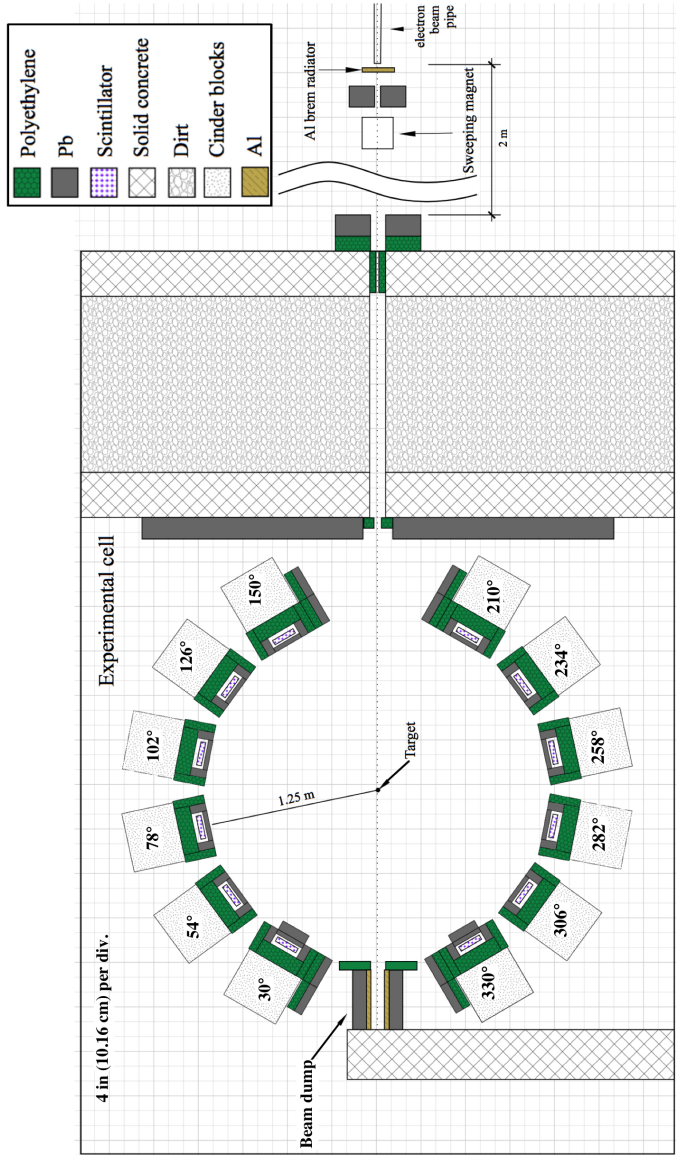


FIG. 2: To-scale, top down diagram of the experimental setup. An electron beam impinges upon a 3.8 cm thick Al radiator, and the resulting bremsstrahlung beam enters the experimental cell from the top. The supporting structure for each detector has been labeled according to the angle, in degrees, between the center of each detector and direction of the incoming photon beam. The fission target, a $0.05 \times 2 \times 4$ cm^3 ^{238}U cuboid, is rotated slowly about the vertical axis in order to mimic the effect of using a cylindrical target.

Ten out of the fourteen scintillators had dimensions of $76.2 \times 15.2 \times 3.8$ cm^3 . The remaining four, the forward-most detectors located at $\pm 30^\circ$ with respect to the beam, had dimensions of $25.4 \times 15.2 \times 3.8$ cm^3 . These scintillators, 1/3 the length of the rest, are the result of the segmentation of two normally sized scintillators in order to address the high photon flux at these locations caused by the forward scattering of photons from the target. Prior to segmentation, a photon was registered in the

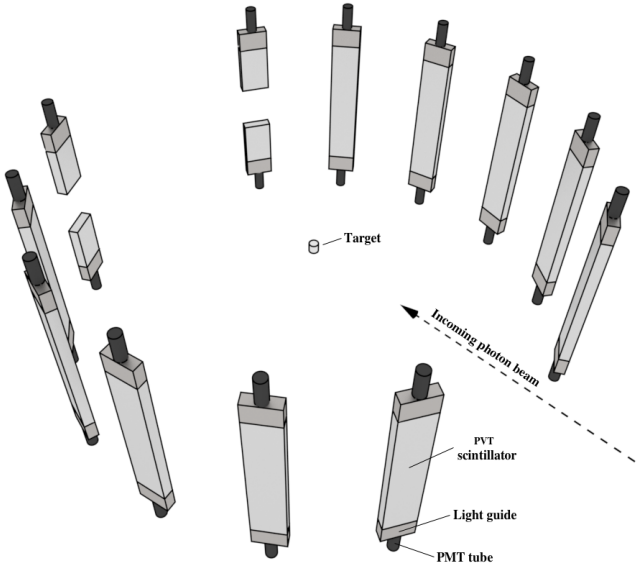


FIG. 3: 3-D rendering of the bare, unshielded scintillators, along with PMTs and light guides. Most of the open space between the scintillators was occupied by shielding, as seen in Fig. 2.

forward-most detectors at a rate of about 0.9 photons per pulse, and because the electronics were operated in single hit mode (see section II E), this greatly reduced the effective neutron detection efficiency. After segmentation and optimization of shielding, the photon detection rate was about 0.2 photons per pulse in each segmented detector. The segmented detectors also differ from the rest in that they were instrumented with only a single PMT, and therefore provide a comparatively lower precision in energy and position measurements. In order to test for systematic errors that may have resulted from the use of the segmented detectors, opening angle measurements were compared with and without their use, and the differences were well within experimental errors.

The relative efficiencies of the neutron detectors as a function of neutron energy were calculated by dividing measured and known yields from the SF of ^{252}Cf taken from MCNP. The results are shown in Fig. 4.

See section IV for a discussion of how the effects of detector efficiency are accounted for in this work.

241
242
243
244
245
246
247
248
249
250
251
252
253
254
255
256
257
258
259
260
261
262
263
264

B. Detector Shielding

The detector shielding, depicted in Fig. 5, was constructed using lead and polyethylene with the aim of reducing detector cross-talk, the detection of photons, and noise. The sides of each scintillator were shielded with 5 cm of lead followed by 5 cm of polyethylene to reduce the chance of neutron cross-talk. Lead was not placed behind the scintillators after an MCNP-POLIMI simulation indicated that cross-talk would occur at significant rates otherwise. Instead, 10 cm of polyethylene was placed be-

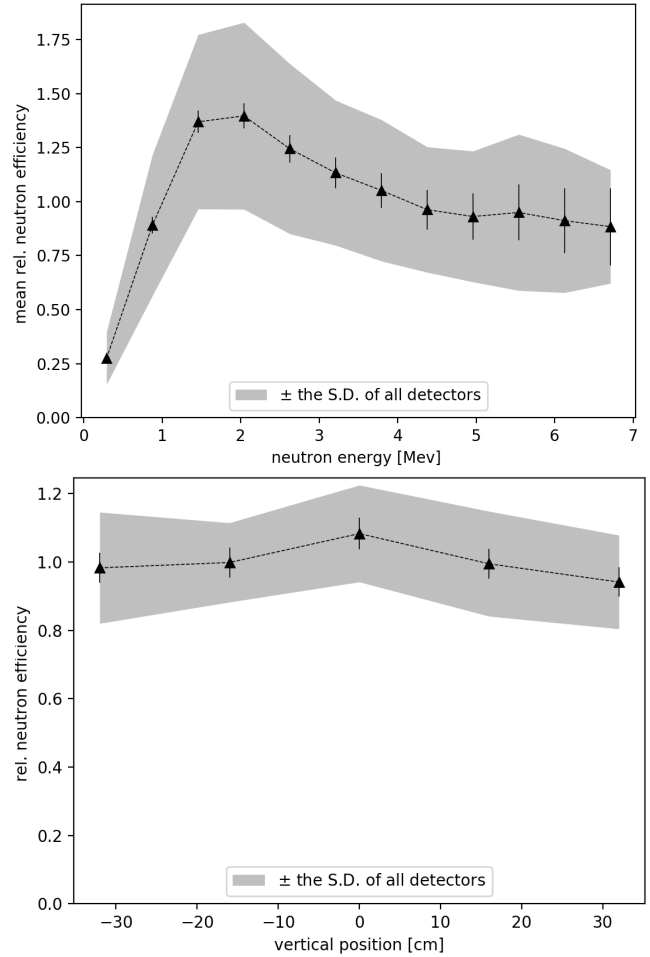


FIG. 4: (top) The mean relative neutron detection efficiency of all detectors as a function of neutron energy is calculated by dividing the measured energy distribution by the known energy distribution of neutrons from the SF of ^{252}Cf . The relative efficiency differs from detector to detector, as demonstrated by the shaded region corresponding to the standard deviation of the relative efficiencies. The error bars represent the uncertainty in the mean. (bot) Mean relative neutron detection efficiency as a function of the reconstructed position along the detectors longest axis.

hind the scintillators. For a detailed discussion about the issue of cross-talk, see section V B.

The front face of each detector was subject to the highest photon flux due to the scattering of the bremsstrahlung beam from the target. The detection of a photon renders the given detector unable to detect any subsequent fission neutrons from the same pulse due to the detector recovery time. Lead mitigates this problem by reducing photon flux, but has the side effect of scattering neutrons. If a neutron scatters prior to being detected, the ToF measurement and position reconstruction are incorrect. The extent of measurement errors caused by lead shielding were quantified using an MCNP simulation, and, accordingly, 2.5 cm of lead was placed

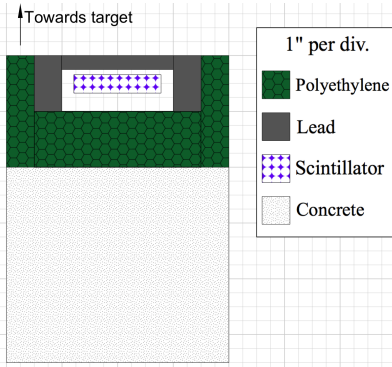


FIG. 5: Detector shielding was designed to reduce the detection of photons, room return, and detector cross-talk.

265 along the front face of the detectors. This diminished
266 photon detection rates to reasonable levels, and, accord-
267 ing to the simulation, leads to a root-mean-square error
268 in opening angle and ToF of 1° and 0.3 ns, respectively,
269 due to neutron elastic scattering.

270 Because of the particularly high photon flux at the
271 sides of all detectors located directly adjacent to the
272 beam, an additional 2" of lead was placed along the sides
273 of these detectors. For the same reason, an additional 2"
274 of lead was also placed along the front faces of the de-
275 tectors farthest downstream, located at $\pm 30^\circ$ from the
276 beam line. The differences in shielding design among the
277 detectors can be seen in Fig 2.

279 C. Bremsstrahlung Photon Beam

280 In order to ensure that all correlated neutrons pro-
281 duced are due to fission, the bremsstrahlung end-point
282 energy was set to 10.5 MeV, safely below the $(\gamma, 2n)$
283 threshold of 11.28 MeV for ^{238}U . Aluminum was chosen
284 for the bremsstrahlung radiator because it has a neu-
285 tron knockout threshold above the energy of the elec-
286 tron beam, which ensured that the radiator would not
287 be a source of fast neutrons with the potential to in-
288 terfere with the experiment. A sweeping magnet was
289 placed downstream from the bremsstrahlung radiator to
290 remove charged particles from the photon beam. Fol-
291 lowing the sweeping magnet, the beam traveled through
292 a series of polyethylene and lead collimators on its way
293 into the experimental cell in which the target was located
294 (see Fig. 2). Figure 6 shows the energy distribution of
295 photons that reach the target according to an MCNP
296 simulation that modeled the collimation and production
297 of the bremsstrahlung photons.

298 The electron beam pulse width was set to 3 ns at a
299 repetition rate of 240 Hz with a 1.1 A peak current. The
300 3 ns pulse width was small compared to the median neu-
301 tron ToF of 80 ns, and thus made a small contribution
302 to the uncertainty in the neutron energy determination.
303

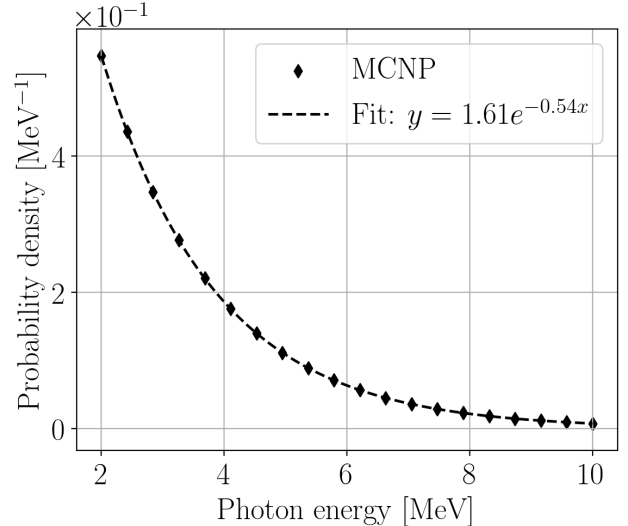


FIG. 6: MCNP simulation of the energy distribution of the bremsstrahlung photons that reach the fission target. Photons with an energy below 2 MeV are excluded.

D. DU Target

305 A depleted uranium (DU) target in the shape of a
306 thin strip with dimensions of $4 \times 2 \times 0.05 \text{ cm}^3$ was used
307 as the primary target. ^{238}U was chosen as the fission
308 target because it is an even-even nucleus, and as a con-
309 sequence, the fission fragments are emitted with a high
310 degree of anisotropy with respect to the photon beam
311 direction [13].

312 Any target comprised of heavy nuclei has a significant
313 potential to scatter fission neutrons before they exit the
314 target. This is a cause for concern, because neutrons
315 that scatter from heavy nuclei are likely to be deflected
316 at large angles, resulting in the measurement of θ_{nn} 's
317 unconnected to the underlying fission kinematics. As
318 discussed in detail in section V C, an MCNP simulation
319 estimated that 6% of reconstructed θ_{nn} 's are perturbed
320 due to neutron scattering within the ^{238}U target. More-
321 over, it is more likely that neutrons emitted along the
322 wide, 2 cm, axis of the ^{238}U target undergo a scattering
323 event than neutrons emitted along the thinnest, 0.05 cm,
324 axis. As a result, detectors located collinear to the widest
325 axis of the target would see relatively fewer neutrons due
326 to increased scattering along this axis. This bias is re-
327 moved by slowly rotating the target about the vertical
328 axis during data acquisition at a rate of one rotation per
329 8 seconds.

E. Electronics

331 A data acquisition system based on the NIM/VME
332 standard was used. A schematic of the data acquisition
333 logic is shown in Figure 8. The PMTs are supplied neg-
334 ative voltages ranging from 1300 to 1500 V by a LeCroy
335

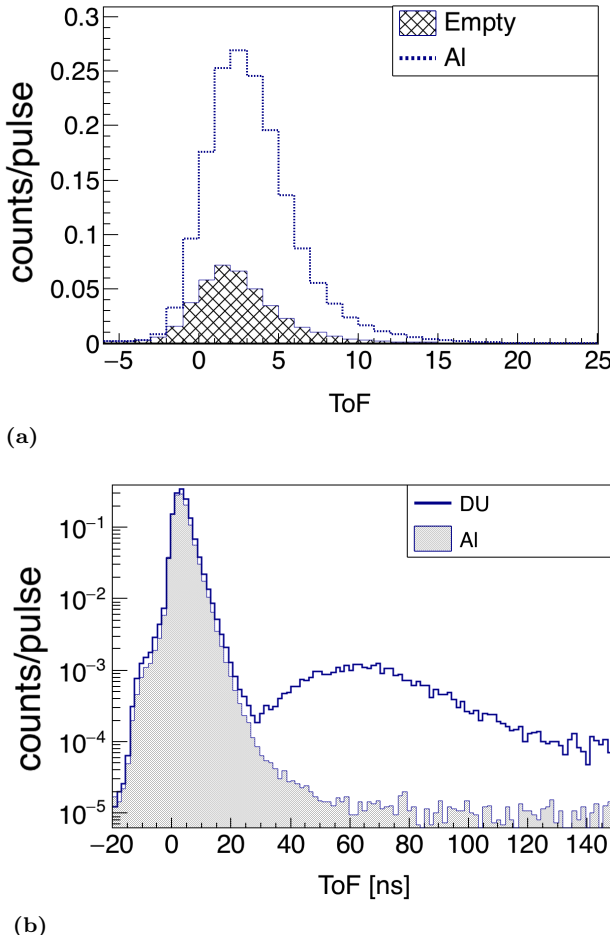


FIG. 7: (a) Comparison between the ToF spectrum of a non-neutron producing target made from Al, to the ToF spectrum produced when no target is in place. The large increase in events around 4 ns is due to photons that scatter from the Al target. When no target is in place, sources of the peak include the collimator leading into the experimental cell and the beam dump. The photon peak seen here is used to find the timing offsets that make it so $t = 0$ corresponds to the moment of fission. (b) Comparison between the Al and DU targets show a pronounced increase in events between 35 and 130 ns due to the introduction of neutrons.

1458 high voltage mainframe. Analog signals from the PMTs were fed into a leading edge discriminator (CAEN Mod. N841) with input thresholds ranging from 30 mV to 50 mV. The threshold and supply voltages were determined individually for each detector to minimize noise, while simultaneously matching the efficiencies of all the detectors as closely as possible. Logic signals from the discriminator were converted to ECL logic and fed into a CAEN model V1290A TDC. The timing of signals from the PMTs were always measured relative to a signal from the accelerator provided at the beginning of each pulse. Even though a multi-hit TDC was used, only the first signal in each pulse from any given PMT was taken into account due to concerns over dead-time within the electronics and signal reflections within the cables. On the

software side, the CODA 2.5 [14] software package developed by Jefferson Laboratory was used to read out the data from the TDC and digitally store it for analysis.

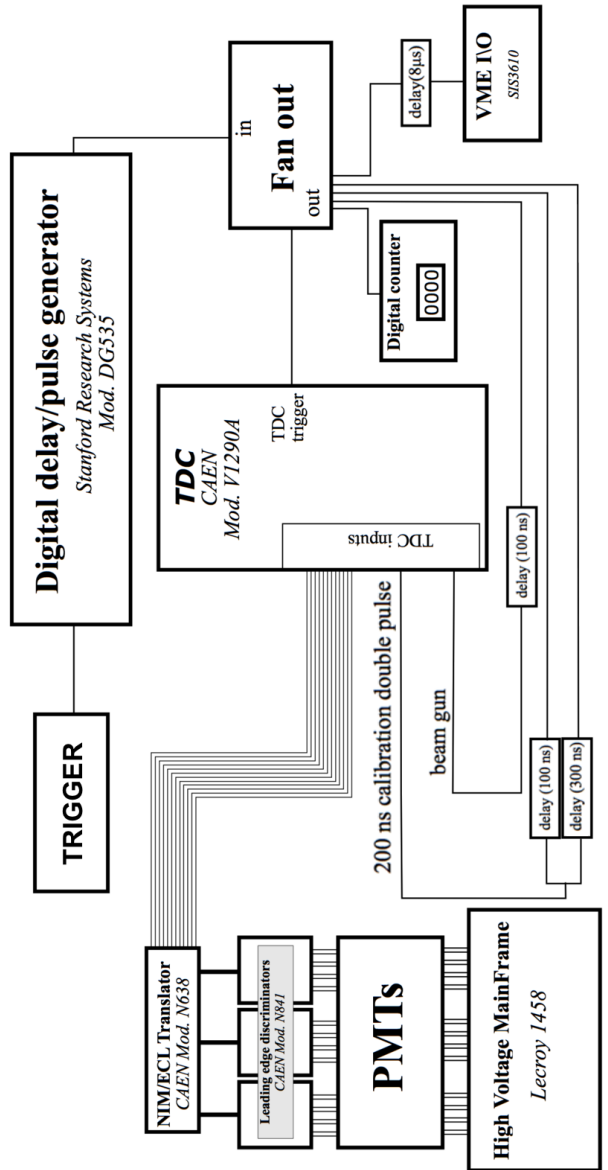


FIG. 8: Wiring diagram of the electronics setup.

III. MEASUREMENT TECHNIQUES

A. Particle Time of Flight and Energy Determination

The ToF of detected particles is used to distinguish between neutrons and photons and to determine neutron energy. A particle's reconstructed position is used to determine direction of motion, which is then used to calculate the opening angle between pairs of detected particles.

362 Position and ToF are each determined using the timing
363 of coincident signals from both PMTs of a given detector.

364 The sum of the times required for scintillation light
365 to travel from the point of scintillation to both PMTs
366 is equal to the time required for the light to travel the
367 full length of the scintillator, which is a constant for light
368 that travels parallel to the length of the scintillator. This
369 is supported by data, shown in Fig. 9, which were pro-
370 duced from a series of tests in which a collimated ^{60}Co
371 source was placed at seven different locations along a
372 scintillator. One of the two coincident photons emitted
373 by ^{60}Co reaches the scintillator and the other is detected
374 by an auxiliary detector serving as the trigger. The pho-
375 tons incident on the scintillator have a spot size of less
376 than 1 cm due to source collimation. These events all
377 have equal transit time, regardless of the ^{60}Co source's
378 position.

379 In Figure 9(a), it can be seen that the time required
380 for the scintillation light to propagate along the scintil-
381 lator has a large effect on the timing of each PMT alone,
382 however, the average of the times of both PMTs is a con-
383 stant, unaffected by the location at which the particle
384 undergoes scintillation. For this reason, taking the aver-
385 age of signals from two PMTs is advantageous because it
386 removes the roughly 5 ns timing error that would other-
387 wise exist due to the time required for scintillation light
388 to propagate along the scintillator. The requirement that
389 there be coincident events in both of a detector's PMTs
390 also aids in reducing noise.

392 During photofission measurements, ToF is calculated
393 by the following expression:

$$\text{ToF} = t_{\text{mean}}^{\text{PMTs}} - t_{\text{beam}} + C, \quad (1)$$

394 where $t_{\text{mean}}^{\text{PMTs}}$ is the mean of the times of signals from
395 both PMTs of a scintillator, t_{beam} is the time of a sig-
396 nal provided by the accelerator at the beginning of each
397 pulse, and C is a constant timing offset. Any process that
398 produces a timing delay that does not change from pulse
399 to pulse contributes to C . For example, the time required
400 for photons to travel from the bremsstrahlung radiator to
401 the target, the propagation of signals through the cables
402 connecting the PMTs, delays in the electronics, etc.

403 The value of C , which may be different for each de-
404 tector, is determined by comparing the timing spectra
405 of the gamma flash produced by a non-neutron produc-
406 ing aluminum target, to that produced when no target is
407 used. The difference between these two spectra reveals a
408 prominent peak in the ToF spectrum due to photons that
409 scatter from the aluminum target. These photons must
410 travel 125 cm to reach the center of any detector and
411 130 cm to reach the top, for which it takes light 4.2 ns
412 and 4.3 ns to travel, respectively. The value of C used for
413 each detector is equal to the value that places the time
414 corresponding to the peak of the target-induced gamma
415 flash at 4 ns.

416 The kinetic energy of a detected neutron is determined
417 straightforwardly from its velocity, which is determined

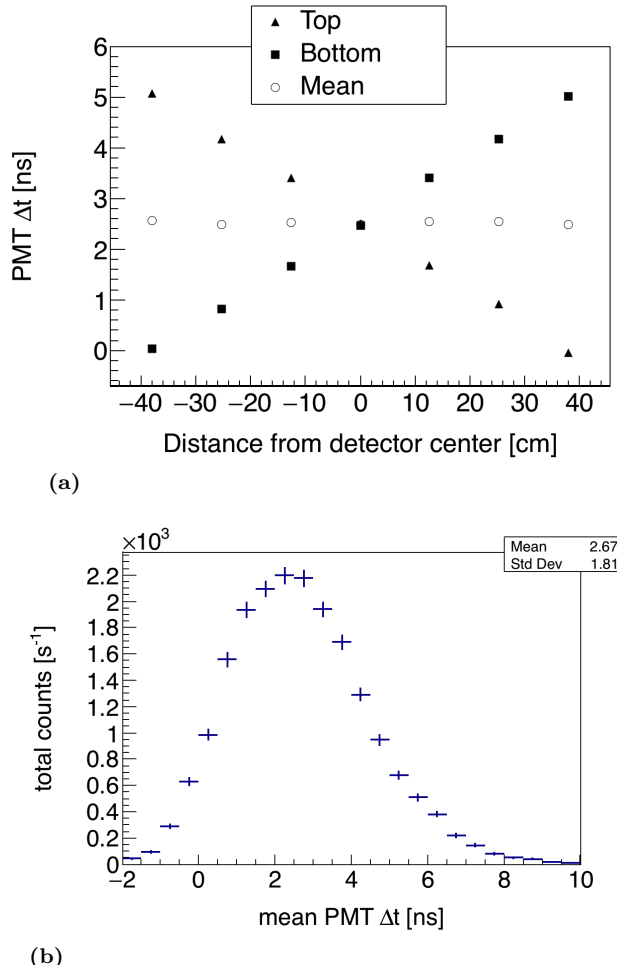


FIG. 9: A collimated ^{60}Co source is used to produce photon events with constant ToF at seven locations along the detector. ^{60}Co produces coincident photons, and one is detected by the scintillator and the other by a separate trigger detector. Δt is the timing of a PMT signal relative to a signal from the trigger detector. In (a), it can be seen that the average between signals from both PMTs does not depend on position. By using the PMT average, there is a reduction in error due to the time required for scintillation light to travel along the scintillator. The uncertainty in ToF measurements is equal to the standard deviation seen in (b), or about ± 2 ns, because all photons from the ^{60}Co source have the same ToF.

418 from its ToF under the assumption that the neutron trav-
419 eled directly from the target to the detectors unimpeded.
420 According to a series of MCNP simulations examining
421 the scattering of fission neutrons within detector shield-
422 ing and the fission target, neutrons predominantly travel
423 to the detectors unimpeded. These simulations are dis-
424 cussed in sections II D and II A.

425

B. Particle Position Reconstruction

426 Each detector is not capable of measuring the position
 427 of a detected particle along the axes parallel to its width
 428 (15.24 cm) or depth (3.81 cm), which contributes $\pm 3^\circ$ to
 429 the total angular uncertainty. The position of a detected
 430 particle along the 76.2 cm length of the scintillator is
 431 calculated using the timing difference of signals from both
 432 of a detector's PMTs. Assuming that scintillation light
 433 travels from an initial point, let it be x cm from the
 434 center of a scintillator, to both PMTs at a velocity that
 435 is constant with respect to the scintillator's length-wise
 436 axis, then the difference between the times at which the
 437 light will reach each PMT (Δt^{PMTs}) is given by:

$$\begin{aligned}\Delta t^{PMTs} &= t^{PMT_1} - t^{PMT_2} \\ &= \frac{(L/2 + x)n_{\text{eff}}}{c} - \frac{(L/2 - x)n_{\text{eff}}}{c} \\ &= 2x \frac{n_{\text{eff}}}{c}.\end{aligned}\quad (2)$$

438 Solving for x gives

$$x = \frac{c}{2n_{\text{eff}}} \Delta t^{PMTs}, \quad (3)$$

439 where t^{PMT_1} and t^{PMT_2} are the times of signals from
 440 each of a detector's PMTs relative to the accelerator gun
 441 pulse, L is the length of the scintillator, c is the speed
 442 of light, n_{eff} is the effective index of refraction of the
 443 scintillation material. A linear least squares fit between
 444 x and Δt^{PMTs} was performed on data gathered using
 445 coincident photons emitted by a collimated ${}^{60}\text{Co}$ source,
 446 as described in the previous section. The resulting fit
 447 parameters, seen in Fig. 10, are used to calculate the
 448 position of detected particles.

450 Using the slope of the linear fit in Fig. 10, along with
 451 Eq. 3, an effective index of refraction of the scintillation
 452 material is calculated to be 2.0. This index of refraction
 453 is said to be "effective" because its measurement is sen-
 454 sitive only to the scintillation light's average speed pro-
 455 jected onto the axis parallel to the scintillator's longest
 456 dimension, which is equal to the intrinsic speed of light
 457 in the material only if the light is traveling parallel to the
 458 scintillator's length. While the detection of scintillation
 459 light by both PMTs favors light paths which are par-
 460 allel or nearly-parallel to the scintillator's length, there
 461 is some reflection of detected scintillation light from the
 462 boundaries of the scintillator. This effect contributes to
 463 the ± 9 cm measurement uncertainty in particle position
 464 reconstruction. As a result of these effects, the index of
 465 refraction measured here is $\sim 25\%$ greater than the true
 466 value of the scintillation material.

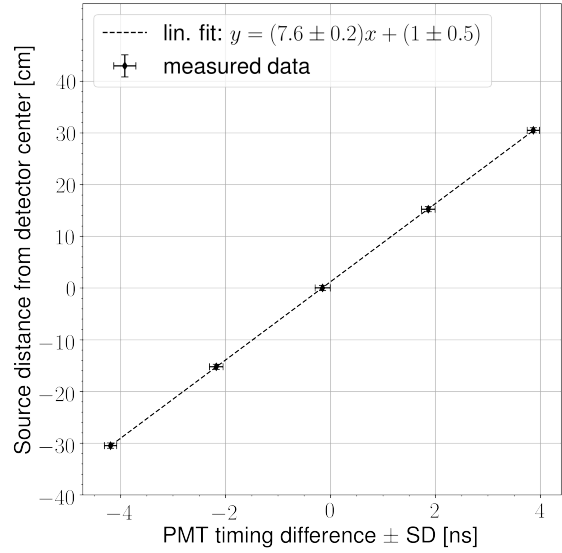


FIG. 10: A collimated ${}^{60}\text{Co}$ source is used to produce photon events at five different positions along the scintillator. The mean PMT timing difference of events at each position varies linearly with respect to the distance of the ${}^{60}\text{Co}$ source from the center of the detector. The result of a linear least squares fit to this data is used to calculate the position of detected particles along the length of each scintillator.

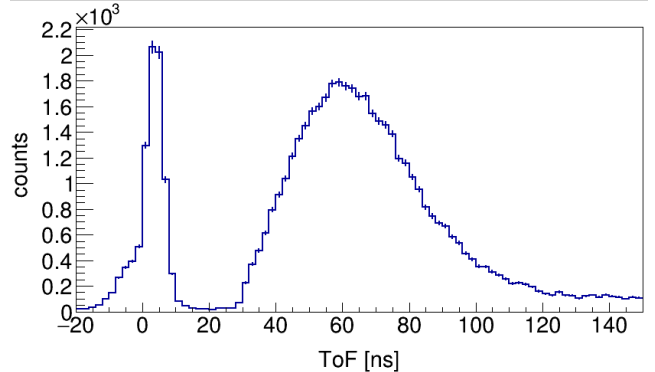


FIG. 11: Measured ToF spectrum from the SF of ${}^{252}\text{Cf}$. The sharp peak on the left is due to fission photons, followed by another peak due to fission neutrons.

467

C. Measurements with ${}^{252}\text{Cf}$

468 A ${}^{252}\text{Cf}$ source was placed at the center of the detec-
 469 tion system shown in Fig. 2 in order to measure the n-n
 470 opening angle distribution. Several such past measure-
 471 ments have been performed (see Refs. [7–10]), and serve
 472 as a means to validate the methods used throughout this
 473 study.

474 The ${}^{252}\text{Cf}$ source produces a cleaner ToF spectrum
 475 than photofission due to the lack of beam related back-

476 grounds (see Fig. 11), and therefore these measurements
 477 have a better signal to noise ratio. Also, there is no con-
 478 cern over the detection of accidental neutron coincidences
 479 because the fission rate of the ^{252}Cf source was about
 480 3,500 fissions/s, making it highly unlikely that multiple
 481 fissions will occur during the electronic acceptance time
 482 window of 150 ns. The beginning of the 150 ns neutron
 483 acceptance time window was triggered by a 2-fold co-
 484 incidence, within a 4 ns window, between two separate
 485 $10 \times 10 \times 5 \text{ cm}^3$ plastic scintillators, one placed above and
 486 the other below the source at a distance of 30 cm. Aside
 487 from this difference in the time window triggering mech-
 488 anism, identical methods were used for both photofission
 489 and SF measurements.

490

IV. ANALYSIS

491 The efficiency and acceptance of the neutron detection
 492 system varies greatly over its opening angle range of 20°
 493 to 180° , as illustrated in Fig. 12. This is both due to the
 494 neutron detection system's non-spherical symmetry and
 495 to varying efficiency as a function of particle position on
 496 the detector. In order to give a result that is sensitive
 497 to angular correlations, but is highly insensitive to detec-
 498 tor efficiencies and experimental drifts in PMT voltage,
 499 accelerator current, *etc.*, the angular correlation is deter-
 500 mined by dividing a correlated neutron distribution by
 501 an uncorrelated neutron distribution. That is,

$$\text{angular correlation} = \frac{nn_{\text{corr}}(\theta)}{nn_{\text{uncorr}}(\theta)}, \quad (4)$$

502 where $nn_{\text{corr}}(\theta)$ is the n-n yield after the subtraction of
 503 accidental n-n coincidences, and $nn_{\text{uncorr}}(\theta)$ is a con-
 504 trived distribution of uncorrelated n-n pairs, which is
 505 produced by pairing neutron events that occurred dur-
 506 ing different pulses. The subtraction of accidental n-n
 507 coincidences to produce $nn_{\text{corr}}(\theta)$ amounts to a 10% cor-
 508 rection, the procedure of which is covered in section IV B.
 509 The construction of $nn_{\text{uncorr}}(\theta)$ is described in detail in
 510 section IV A.

511 **A. Cancelation of Detector Efficiencies, Drifts, and
 512 Geometric Phase Space**

513 The construction of $nn_{\text{uncorr}}(\theta)$ is achieved by pairing
 514 detected neutrons that were produced during different ac-
 515 celerator pulses. The same set of pulses used for $nn_{\text{corr}}(\theta)$
 516 is used here, so each of these pulses individually consist
 517 of the detection of two coincident neutrons. When con-
 518 structing $nn_{\text{uncorr}}(\theta)$, it is desirable that the neutrons
 519 comprising each uncorrelated n-n pair originated from
 520 different pulses that occurred as closely together in time
 521 as possible. A smaller time difference between pulses
 522 that are paired for this purpose increases the chance that
 523 both neutrons were detected under the same experimen-

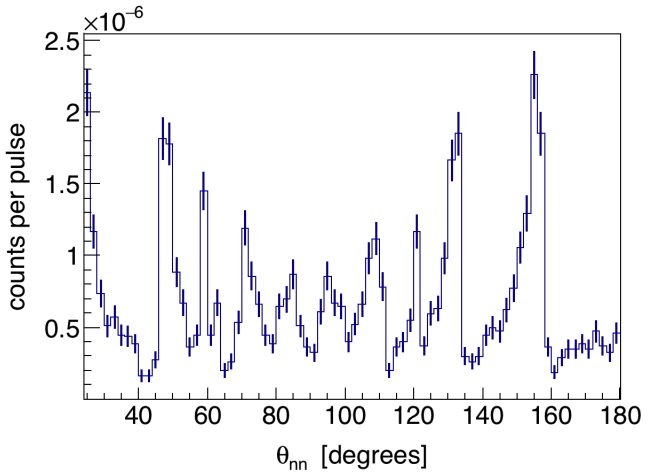


FIG. 12: Raw n-n opening angle yield from the photofission of ^{238}U . This distribution is highly influenced by the detection system's geometric acceptance and efficiency.

524 tal conditions amid any drifting of accelerator current,
 525 PMT voltages, and varying rates of noise. However, some
 526 time difference between the pulses must be allowed so as
 527 not to cause insufficient counting statistics. Accordingly,
 528 uncorrelated n-n pairs used to construct $nn_{\text{uncorr}}(\theta)$ are
 529 formed by neutrons that were detected within 30 minutes
 530 or less of each other.

531 Uncorrelated n-n pairs will have a slightly different
 532 joint energy distribution than correlated n-n pairs, which
 533 could affect the extent to which the effects of detector
 534 efficiency cancel in Eq. 4. This issue is addressed in sec-
 535 tion V A, where it is shown that these differences have
 536 little potential to significantly affect the final result.

537 Figure 13(a) shows the measured yield distribution of
 538 correlated neutrons, $nn_{\text{corr}}(\theta)$, from the photofission of
 539 ^{238}U . The structure seen here is reflective of the under-
 540 lying n-n angular correlations as well as the geometric
 541 acceptance and efficiencies of the neutron detectors. Fig-
 542 ure 13(b) reveals how a clear picture of n-n angular corre-
 543 lations emerges when taking the ratio between $nn_{\text{corr}}(\theta)$
 544 and $nn_{\text{uncorr}}(\theta)$.

546 **B. Subtraction of Accidental Coincidences**

547 The observation of two uncorrelated signals in the neu-
 548 tron ToF range, whether caused by neutrons, photons,
 549 or noise, is referred to as an *accidental coincidence*. Ac-
 550 cidental coincidences due to noise and photons, which
 551 are estimated using a non-neutron producing aluminum
 552 target (see Fig. 14), amount to about 3% of all coin-
 553 cidences. Accidental coincidences due to neutrons are
 554 minimized by adjusting the accelerator's current so that
 555 there are, on average, less than 1.0 fissions per accelerato-
 556 r pulse. Nevertheless, statistical fluctuations in the num-
 557 ber of fissions per pulse result in the production of acci-
 558 dental coincident neutrons that originated from different,

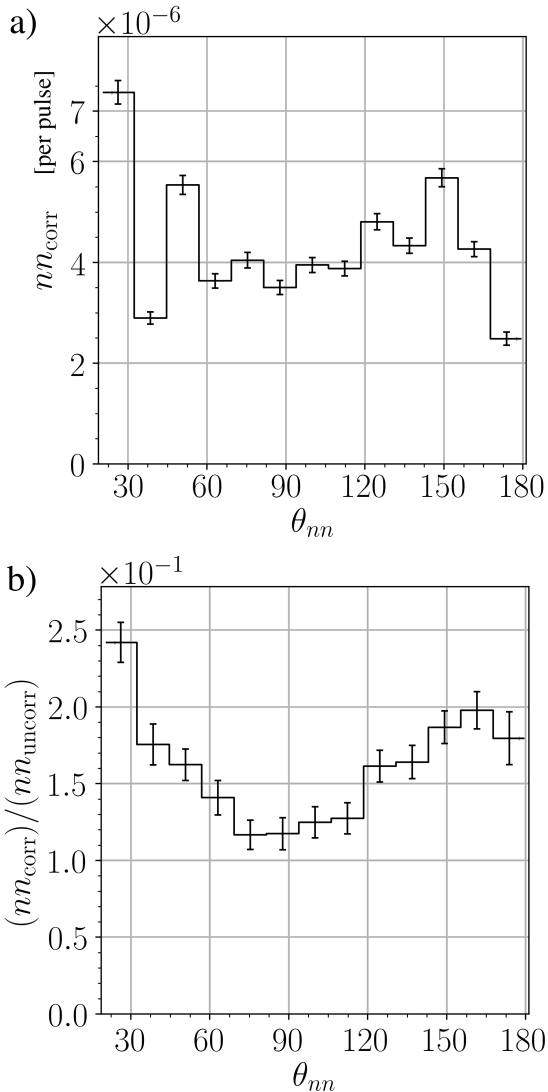


FIG. 13: n-n opening angle distribution from the photofission of ^{238}U before the normalization procedure seen in Eq. 4 (a), and after normalization (b). All measured neutrons have an energy greater than 0.4 MeV.

and therefore, uncorrelated fissions. There are also accidental neutron coincidences caused by the occurrence of multiple (γ, n) reactions in a single pulse. The energy integrated (γ, n) cross-section of ^{238}U , weighted by the bremsstrahlung energy distribution, is about a factor of 5.5 times greater than it is for photofission (see Fig. 15). As a result, the raw n-n coincident yield will contain a significant number of n-n coincidences from multiple (γ, n) reactions in relation to n-n coincidences from fission. The presence of accidental n-n coincidences has the effect of washing out the signal from correlated neutrons.

The raw measurement of n-n yield consists of a mix of

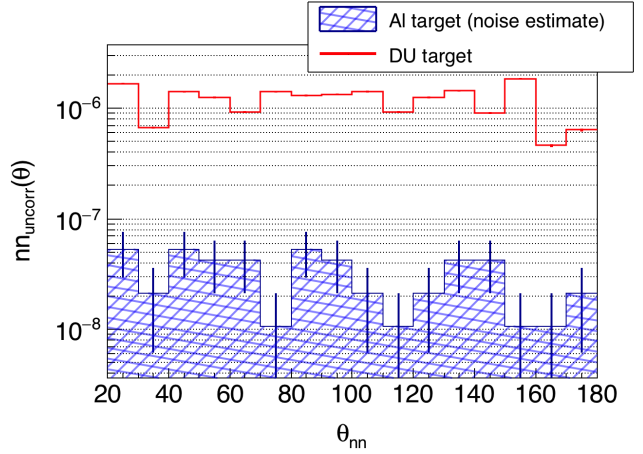


FIG. 14: An Al target was designed have the same thickness, in radiation lengths, as the ^{238}U target, thus serving as an equivalent non-neutron producing target well-suited for noise estimates. The rate of the detection of coincident events in the neutron ToF range while using the Al target was 3% that of the ^{238}U target. Thus, 3% of coincident events used in the determination of n-n angular correlations in ^{238}U can be attributed to noise.

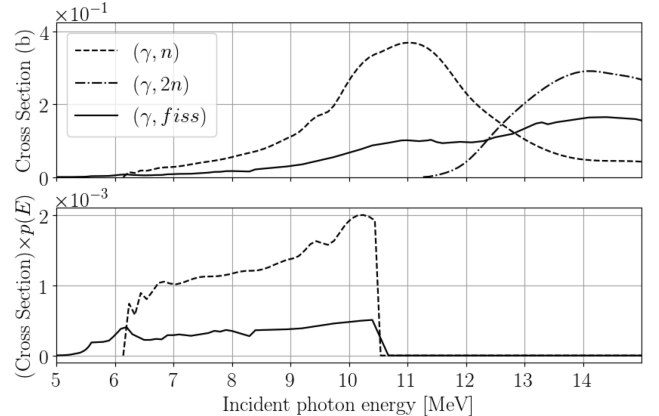


FIG. 15: (top) ENDF cross-sections of (γ, fiss) , direct (γ, n) , and direct $(\gamma, 2n)$. (bottom) Cross-sections weighted by the simulated relative rate of bremsstrahlung photons that reach the target as a function of photon energy. The integrated cross-sections of (γ, n) is 5.5 times greater than for (γ, fiss) . Assuming a $\bar{\nu}$ of 2 neutrons/fission, the bremsstrahlung beam produces about 2.7 times more neutrons via (γ, n) than (γ, fiss) within the target.

correlated and accidental neutron coincidences, that is

$$nn_{\text{raw}}(\theta_{nn}) = nn_{\text{corr}}(\theta_{nn}) + nn_{\text{acc}}(\theta_{nn}), \quad (5)$$

where $nn_{\text{raw}}(\theta_{nn})$ and $nn_{\text{acc}}(\theta_{nn})$ are the per-pulse n-n yields as a function of opening angle, θ_{nn} , for all detected n-n pairs, and detected accidental n-n pairs, respectively. As already defined, $nn_{\text{corr}}(\theta_{nn})$ is the per-pulse yield of detected correlated n-n pairs.

Because the n-n coincidences comprising $nn_{\text{acc}}(\theta_{nn})$

580 consist of two independent detected neutrons, they are
 581 governed by the exact same physics and are subject to
 582 the exact same experimental conditions as n-n coinci-
 583 dences formed by pairing of single neutrons that were
 584 detected during different pulses. Therefore, the open-
 585 ing angle distribution formed by pairing neutrons that
 586 were detected during different pulses, denoted $nn_{dp}(\theta_{nn})$,
 587 is proportional to $nn_{acc}(\theta_{nn})$. $nn_{dp}(\theta_{nn})$ is constructed
 588 from the set of all possible pulse-pairs formed by pulses
 589 that occurred within 0.2 seconds of each other. The re-
 590 striction in time difference is applied in order to increase
 591 the chance that pulse pairs together occurred under sim-
 592 ilar experimental conditions. There are no other restric-
 593 tions on which pulses can be used in this case. Thus,
 594 many pulse-pairs used for the construction of $nn_{dp}(\theta_{nn})$
 595 will contain no detected neutrons.

596 While $nn_{dp}(\theta_{nn})$ and $nn_{acc}(\theta_{nn})$ are proportional,
 597 $nn_{acc}(\theta_{nn})$ is not equal to $nn_{dp}(\theta_{nn})$, because there are,
 598 on average, more detected neutrons per pulse-pair than
 599 per pulse. As the following analysis shows, $nn_{acc}(\theta_{nn}) =$
 600 $\frac{1}{2}nn_{dp}(\theta_{nn})$, under the condition that $nn_{acc}(\theta_{nn})$ is nor-
 601 malized to the number of pulses and $nn_{dp}(\theta_{nn})$ to the
 602 number of pulse-pairs looked at. When looking at single
 603 pulses, the probability of there being a detected uncorre-
 604 lated n-n pair is denoted by P_{sp}^{n-n} , and when looking at
 605 pulse-pairs, by P_{dp}^{n-n} . Thus, P_{sp}^{n-n} and P_{dp}^{n-n} determine the
 606 relative rates of $nn_{acc}(\theta_{nn})$ and $nn_{dp}(\theta_{nn})$, respectively.

607 The statistics of the detected uncorrelated neu-
 608 trons per pulse is assumed to follow a Poisson distribu-
 609 tion, which describes the occurrence of independent ran-
 610 dom events. Accordingly, the probability of the detection
 611 of k uncorrelated neutrons in a given pulse is

$$612 p(k) = \frac{e^{-\lambda}\lambda^k}{k!}, \quad (6)$$

612 where λ represents the mean number of uncorrelated de-
 613 tected neutrons per pulse. In principle, λ equals the total
 614 number of detected uncorrelated neutrons divided by the
 615 total number of pulses. Determination of λ cannot be
 616 done in practice, because one would need to know which
 617 pairs of detected neutrons are correlated. However, the
 618 largest possible value for λ is the total number of de-
 619 tected neutrons divided by the total number of pulses, as
 620 this quantity counts all detected neutrons, whether they
 621 are correlated or uncorrelated. For this work, that places
 622 an upper bound on λ of 5.5×10^{-3} detected uncorrelated
 623 neutrons per pulse, which is small enough to truncate all
 624 terms beyond the leading term in the following analysis.

625 Because P_{sp}^{n-n} represents the probability of the detec-
 626 tion of two uncorrelated neutrons in a single pulse, P_{sp}^{n-n}
 627 is equal to $p(2)$, as per Eq. 6. Thus,

$$628 P_{sp}^{n-n} = \frac{e^{-\lambda}\lambda^2}{2!} \\ 629 \approx \frac{\lambda^2}{2} + \mathcal{O}(\lambda^3). \quad (7)$$

When considering the case of P_{dp}^{n-n} , recall that, in
 this case, uncorrelated n-n pairs are formed by exam-
 ining pulse-pairs. Here, an uncorrelated n-n pair occurs
 when there is a detected neutron in both pulses. Because
 all terms beyond the leading term are being truncated,
 pulse-pairs in which one or both of the pulses comprise
 two or more detected neutrons do not need to be con-
 sidered. Thus, P_{dp}^{n-n} is equal to the probability of there
 being exactly one detected neutron in each pulse, which
 is the square of the probability of there being exactly one
 detected neutron in a single pulse, namely, $p(1)^2$. Thus,
 again using Eq. 6,

$$P_{dp}^{n-n} = (e^{-\lambda}\lambda)^2 \\ \approx \lambda^2 + \mathcal{O}(\lambda^3). \quad (8)$$

Because P_{dp}^{n-n} and P_{sp}^{n-n} determine the relative rates of
 $nn_{dp}(\theta_{nn})$ and $nn_{acc}(\theta_{nn})$, respectively, and because the
 two distributions have the same shape, from Eq.'s (8)
 and (7), it follows that

$$nn_{acc}(\theta_{nn}) = \frac{1}{2}nn_{dp}(\theta_{nn}). \quad (9)$$

Finally, from Eq.'s 9 and 5, the distribution of solely
 correlated n-n pairs can be recovered from the raw mea-
 surement as follows

$$nn_{corr}(\theta_{nn}) = nn_{raw}(\theta_{nn}) - \frac{1}{2}nn_{dp}(\theta_{nn}). \quad (10)$$

V. POTENTIAL SOURCES OF ERROR

A. Correlated versus uncorrelated n-n energy distribution

In order to effectively minimize the dependence of the
 result on detector geometry/efficiency, the numerator
 and denominator of Eq. 4 must comprise neutron pairs
 with a similar energy distribution. Note that accidental
 coincident neutrons from (γ, n) are completely removed
 from $nn_{corr}(\theta)$, the numerator in Eq. 4, by the subtrac-
 tion of accidental coincidences, but are not removed from
 the denominator, $nn_{uncorr}(\theta)$. This is the reason for us-
 ing only pulse-pairs that have two events in each pulse
 when determining the uncorrelated neutron distribution.
 Doing so increases the selection of neutrons from fission
 as opposed to (γ, n) .

When examining differences between the neutron en-
 ergy distributions in $nn_{corr}(\theta)$ and $nn_{uncorr}(\theta)$, it is im-
 portant to consider how the energies of both neutrons
 forming n-n pairs vary together, or, in other words, their
 joint energy distribution. Figure 16 shows the ratio be-
 tween the rates for correlated and uncorrelated n-n pairs
 of various binned energies. The effect that these dis-
 crepancies in energy distribution have on the final result
 can be examined by applying a weighting factor to each
 event in $nn_{uncorr}(\theta)$ such that a recalculation of the re-

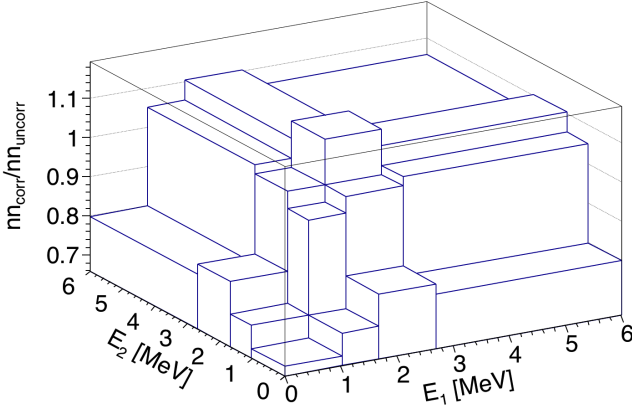


FIG. 16: The z-axis represents the ratio between the correlated and uncorrelated rates of binned n-n energies. The energy bins are chosen such that each contains an equal number of events, or 1/16th of the total events.

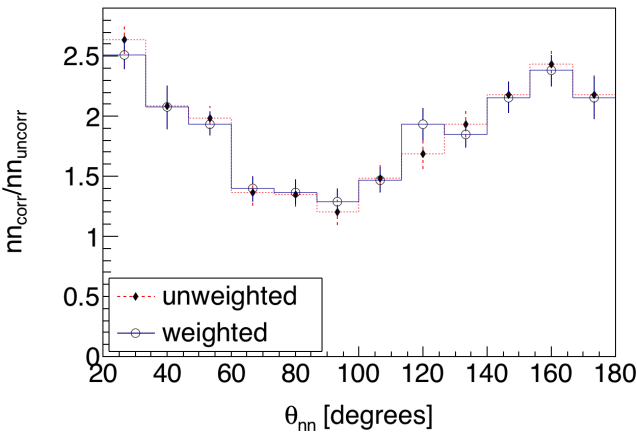


FIG. 17: Each uncorrelated n-n event can be weighted such that the weighted histograms of the joint n-n energy distributions of correlated and uncorrelated n-n pairs are equal. Comparison of the calculated angular correlation results, with and without such weighting factors applied to all uncorrelated n-n events, illustrates that any effects due to the discrepancies in the joint energy distributions of correlated and uncorrelated n-n pairs are negligible.

672 sult in Fig. 16 produces a flat curve. A comparison of
673 the determined angular correlation with and without the
674 application of these weighting factors to all uncorrelated
675 n-n events is seen in Fig. 17. The resulting differences in
676 angular correlation are negligible.

679

B. Detector Cross-talk

680 *Cross-talk* occurs when, after a particle is detected
681 once, the same particle, by any means, causes a detec-
682 tion to be registered in a different detector. For example,
683 upon detection, a particle may undergo elastic scattering
684 and then travel into another detector where it is detected
685 again, or, it may produce secondary particles that are

686 detected. The two coincident detections of a cross-talk
687 event are causally correlated, and thus they have the po-
688 tential to contaminate the signal from correlated fission
689 neutrons. If both detections occur during the ToF range
690 typical for fission neutrons, then the cross-talk event can-
691 not be distinguished from the detection of two correlated
692 neutrons.

693 Recent works that measured the n-n angular correla-
694 tions in the spontaneous fission of ^{252}Cf and ^{240}Pu [8, 12]
695 addressed this effect by using an MCNP-PoLiMi simula-
696 tion to estimate and then subtract cross-talk from their
697 measurements. In this work, the issue of cross-talk is
698 approached differently by employing the use of detector
699 shielding aimed at reducing cross-talk to a negligible rate.
700 By using shielding to reduce cross-talk, this measurement
701 is less dependent on the details of the models used by
702 MCNP-PoLiMi to simulate neutron transport and detec-
703 tion. MCNP-PoLiMi simulations are used in this work
704 only to verify that the effect of cross-talk is negligible.

705 The scintillators used here are much larger than those
706 used in similar works, such as in Refs. [8, 12], allowing
707 them to be placed much farther from the fission source
708 without causing a detrimental loss in coincidence rates.
709 An increase in the distance between the detectors and the
710 fission source makes this measurement less subject to to
711 angular uncertainty, which depends directly on the un-
712 certainty in the position of a detected particle due to, for
713 example, the scattering of neutrons from detector shield-
714 ing. For this reason, larger amounts of shielding can be
715 used without concern of introducing large errors.

716 Furthermore, the geometry of the neutron detection
717 system makes it kinematically impossible for a neutron
718 to undergo a single scattering event with a proton in one
719 detector, which is the basis for scintillation, and then
720 travel directly into another detector with enough kinetic
721 energy to be detected a second time. For this reason,
722 upon being detected, a neutron must scatter from one or
723 more intermediate nuclei, such as lead or carbon, in or-
724 der for it to reach another detector with enough energy
725 to be detected again. This fact follows from the con-
726 servation of energy and momentum. In order to support
727 the claim that the design of the neutron detection system
728 reduced cross-talk to negligible rates, a detailed MCNP-
729 PoLiMi [15] simulation was performed in which a built-in
730 ^{252}Cf source is positioned at the center of a model of the
731 neutron detection system.

732 1. Simulation of Detector Cross-talk

733 The cross-talk simulation included all scintillators,
734 shielding, detector supporting structures, and the con-
735 crete walls surrounding the experimental cell. MCNP-
736 PoLiMi's built-in ^{252}Cf spontaneous fission source was
737 used, which emits neutrons with the correct corre-
738 lations and multiplicities according to previous measure-
739 ments. Detector response was modeled using a program
740 included with the MCNP-PoLiMi distribution called MP-

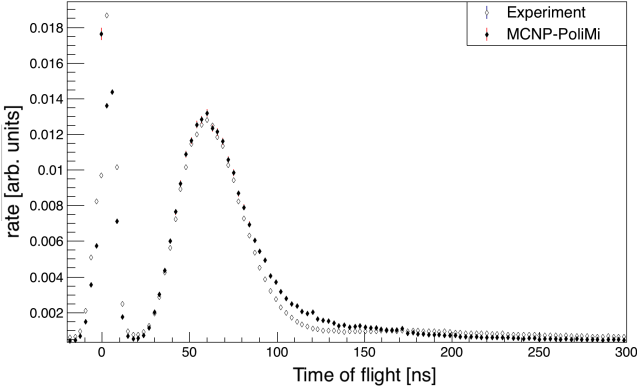


FIG. 18: Measured versus simulated ToF spectrum from the SF of ^{252}Cf . The simulation used the detector response model outlined in ref [16]. The simulated and measured curves are normalized in order to facilitate comparison.

741 Post [16]. The model is based on the MeV electron equiv-
 742 alent (MeVee) light output produced by particles as they
 743 undergo collisions with carbon and hydrogen within or-
 744 ganic plastic scintillators. A minimum deposited energy
 745 of 0.4 MeV (equivalent to 0.05 MeVee for neutrons) was
 746 assumed for detectable particles, which was chosen be-
 747 cause the neutron detection system exhibited a sharp de-
 748 cline in detection efficiency for neutrons below 0.4 MeV.

749 For neutron collisions with hydrogen, the light output
 750 in MeVee, denoted L , is calculated by the following em-
 751 pirically derived formula [16]

$$L = 0.0364\Delta E_n^2 + 0.125\Delta E_n,$$

752 where ΔE_n is equal to the loss in the kinetic energy of the
 753 neutron due to the collision. Neutron interactions with
 754 carbon are assumed to generate a small light output of

$$L = 0.02\Delta E_n.$$

755 As seen in Fig. 18, this model of the detection process
 756 produces a ToF spectrum for the SF of ^{252}Cf that shows
 757 good agreement with the measurement for neutrons with
 758 a ToF less than 100 ns and fair agreement for neutrons
 759 with a ToF greater than 100 ns.

760 Figure 19 shows the distribution of cross-talk events
 761 and true n-n coincidences as a function of reconstructed
 762 opening angle. It is worth noting that, according to this
 763 simulation, the effect of cross-talk is not only small, but is
 764 also distributed over a wide range of angles rather than
 765 being concentrated around 0 degrees as one might ex-
 766 pect. Angles greater than 125 degrees are not shown
 767 in Fig. 19 because cross-talk events at large angles can
 768 be readily identified in analysis due to the large amount
 769 of time required for a neutron to travel these distances.

770 The simulation was initially performed with 5 cm of lead
 771 shielding placed behind the scintillators, and the num-
 772 ber of cross-talk events accounted for 11% of the total
 773 coincident neutron events. This value fell to 3% when

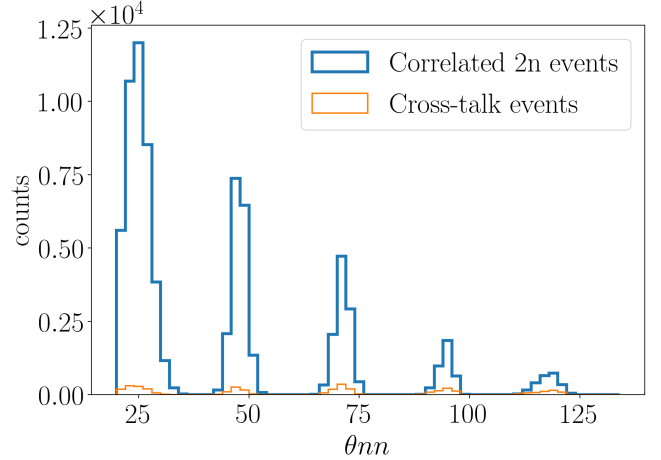


FIG. 19: MCNP-PoLiMi simulation of the number of cross-talk events versus correlated n-n events as a function of reconstructed opening angle. Cross-talk accounted for 3% of total events. Simulated cross-talk events do not occur primarily at small angles, but are instead spread out over a wide range of angles. Any cross-talk occurring at angles larger than 125° will be removed from the experimental data by the cuts applied to neutron ToF.

775 polyethylene was used instead of lead, motivating the
 776 placement of 10 cm of polyethylene behind the detectors
 777 instead of lead.

C. Neutron Scattering within the Target

778 A potential source of error in opening angle measure-
 779 ments is the scattering of emitted neutrons as they tra-
 780 verse the fission target. This is a cause for concern be-
 781 cause when neutrons scatter from heavy nuclides such
 782 as ^{238}U , they are likely to be deflected at large angles
 783 resulting in n-n opening angles that do not reflect the
 784 true underlying fission kinematics. The effect that this
 785 has on this work is assessed by MCNP simulations. In
 786 summary, for 6% of n-n pairs, at least one neutron out
 787 of the two scatters before exiting the target, according to
 788 the simulation. This effect does not have a large influ-
 789 ence on the measured θ_{nn} distribution according to the
 790 simulation data shown in Fig. 20.

791 The rate of elastic scattering is affected by the size
 792 and shape of the target. A thin strip is the ideal target
 793 shape regarding the rate of neutron elastic scattering per
 794 unit of total target volume. See Fig. 21 for the simulated
 795 elastic scattering rates for both thin strip and cylindrical
 796 shaped targets. The simulation indicated that the rate of
 797 elastic scattering in cylindrical targets is about a factor
 798 of two times greater than in thin strip targets with the
 799 same volume.

800 The target's dimensions are small enough that the
 801 rate of photon absorption, and thus photo-neutron pro-
 802 duction, is virtually uniform throughout the entire tar-
 803 get volume. An MCNP-PoLiMi simulation was used

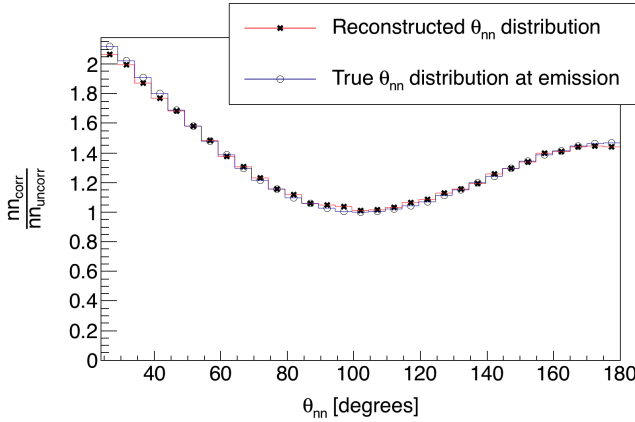


FIG. 20: MCNP-PoLiMi simulation of correlated ^{252}Cf neutrons sampled uniformly throughout a $0.05 \times 2 \times 4 \text{ cm}^3$ U-238 target. The slight difference between the curves is due solely to the elastic scattering of neutrons within the target, since detector physics was not simulated. In the reconstructed θ_{nn} distribution (\star), only neutrons which enter a physical volume at which a detector was located during the experiment are counted. The true θ_{nn} distribution at the moment of emission is also plotted (\circ).

to generate ^{252}Cf spontaneous fission events uniformly throughout the target. The SF of ^{252}Cf is used instead of the photofission of ^{238}U because of the current lack of photofission models, however, the underlying fission kinematics are, broadly speaking, the same for the SF of ^{252}Cf and the photofission of ^{238}U . Thus, the two processes have similar n-n correlations.

Section VIB discusses the observation of an unexpected drop in correlation around 180° in our photofission of ^{238}U measurement, as seen in Figs. 22 and 23. This motivated a second simulation regarding elastic scattering which examined whether this decrease in the correlation around 180° opening angles reflects the underlying physics of the fission process. In particular, note that throughout these measurements, the target was continuously rotated once per 8 seconds. This means that for the determination of the uncorrelated opening angle distribution, the trajectories of the two neutrons were taken from two different pulses in which the target was at a different orientation for each of them. Additionally, each of the neutrons likely originated from different regions of the target volume. On the other hand, for the same-pulse, correlated neutron measurement, the target was in the same orientation and the two neutrons were generated at the same position in the target. For these reasons, the rates of neutron scattering within the target are not necessarily equal for the same-pulse and different-pulse cases. As such, we investigated whether these differences could cause this apparent decrease in the opening angle distribution near 180° .

Using the correlated ^{252}Cf SF source built-in to MCNP-PoLiMi, the opening angle distribution of neutrons at the moment of emission, labeled *true* in Fig. 20,

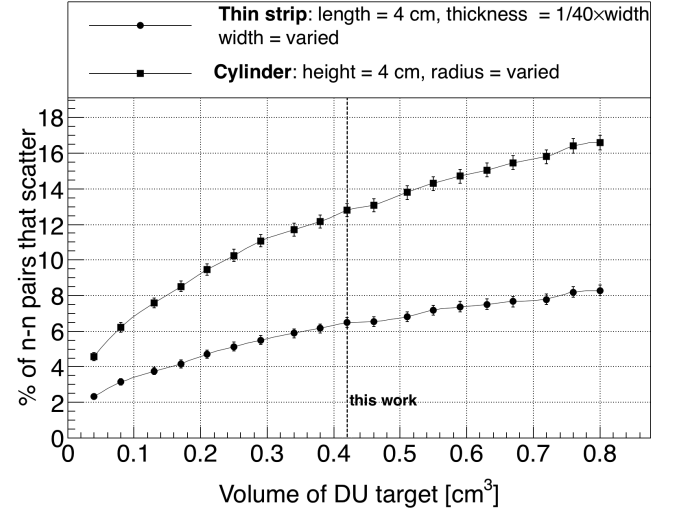


FIG. 21: Result of an MCNP simulation in which n-n pairs, with energies sampled from a typical watt fission spectrum, were generated uniformly throughout the volume of DU targets. The y-axis is the rate of opening angle contamination due to the scattering of, within the DU target in which they were produced, either one or both of a pair of neutrons. The lack of symmetry of a thin strip target can be removed by slowly rotating the target around the vertical axis during data acquisition, making it the optimal target geometry for the minimization of the rate of neutron scattering. The target used in this work had a length of 4 cm, a width of 2 cm, and a thickness of 0.05 cm.

were compared to that of the neutrons after they have escaped the target, labeled *reconstructed* in Fig. 20. The location of fission events were sampled uniformly throughout the target's volume. The analysis employs the same technique outlined in section IV A, in which a correlated neutron distribution is divided by an uncorrelated neutron distribution. The correlated neutron distribution is formed by pairing neutrons emitted during the same fission, and the uncorrelated distribution by the pairing of neutrons emitted during different fissions. In order to account for the effect of a rotating target on the trajectories of neutrons from different-pulses, the coordinate system was rotated about the vertical axis accordingly for different fission events. The result from this simulation suggests that the rotating $0.05 \times 2 \times 4 \text{ cm}^3$ U-238 target does not, due to neutron scattering, result in a measurable departure from the true n-n opening angle distribution.

VI. RESULTS

The n-n opening angle correlation is calculated using the methods outlined in Sec. IV, in which a correlated neutron yield is divided by an uncorrelated yield. The results are compared with output from FREYA [17] (Fission Reaction Event Yield Algorithm), which was developed by the collaborative efforts of researchers from

866 Lawrence Berkeley National Laboratory, Lawrence Livermore National Laboratory, Los Alamos National Laboratory, and University of Michigan Nuclear Engineering, and has been included in MCNP beginning with version
 870 6.2.

871 The most recent release of FREYA (version 2.0.3)
 872 does not model photofission directly, but instead uses
 873 a neutron-induced fission model as an *ad hoc* photofission model [18]. Modeling photofission in this manner is
 874 a crude approximation, unbacked by experimental verifica-
 875 tion. Nonetheless, due to the current lack of accepted
 876 photofission models, the approximate model included in
 877 FREYA version 2.0.3 is compared with the results of the
 878 present work.

880 For a given nucleus with Z protons and A total nucle-
 881 ons, the code selects the neutron-induced fission model
 882 for a Z(A-1) nucleus, and chooses an incident neutron
 883 energy such that the compound ZA nucleus will have,
 884 relative to ZA's ground state, an excitation energy that
 885 is equal to the energy of the would-be incident photon.

886 When using FREYA to model photofission in this
 887 work, all model parameters, such as level density and
 888 partition parameters, were set to their default values for
 889 neutron-induced fission. FREYA was configured to use
 890 the fission fragment mass distribution, $Y(A)$, and the
 891 average total kinetic energy, $\langle \text{TKE} \rangle(A)$, from the ^{238}U
 892 photofission measurements described in Ref. [19].

893 A. n-n angular correlation versus neutron energy

894 The measured θ_{nn} distribution from the photofission of
 ^{238}U and the SF of ^{252}Cf are presented with the following
 895 two different types of cuts applied to the energies of neu-
 896 trons in coincidence: in Figs. 22 (^{238}U) and 24 (^{252}Cf), a
 897 minimum energy threshold is applied to both neutrons,
 898 and in Figs. 23 (^{238}U) and 25 (^{252}Cf), the energy of both
 899 neutrons are required to fall within a specified range
 900

901 In each of Figs. 22 through 25, the data are reported
 902 using two representations: the classic histogram and the
 903 kernel density estimate (KDE). When using a histogram
 904 to estimate a continuous distribution from the relatively
 905 small number of data points obtained in this work, one
 906 faces the following dilemma: small bin-widths lead to
 907 large uncertainties that are dependent on the chosen bin-
 908 width, while large bin-widths obscure potentially useful
 909 information. This problem is mitigated by the use of a
 910 KDE. A KDE is a method for estimating a continuous
 911 probability distribution from a finite set of sampled data
 912 points. The kernel was chosen to be the measurement
 913 errors in opening angle as determined by a study using
 914 coincident photons from a ^{60}Co source, which was placed
 915 at different locations along a detector. The measurement
 916 errors in θ_{nn} are well-described by a gaussian with a stan-
 917 dard deviation of 6° . Mathematical details of the KDE
 918 method used in this work are outlined in Ref. [20]. The
 919 error bands seen in Figs. 22 through 25 correspond to
 920 68% confidence intervals.

921 Plotted alongside each measurement is the result of
 922 a FREYA simulation. For the measurement of ^{238}U
 923 photofission, there were a total of 2,952 n-n coincident
 924 events after the subtraction of accidentals, and for the
 925 SF of ^{252}Cf , there were 21,882.

926 B. Considering θ_{abs}

927 While the results reported in the previous section are
 928 consistent with the effect of the kinematic focusing of the
 929 neutrons due to the recoil of the fission fragments, the
 930 data for U-238 show a statistically significant decrease
 931 in the n-n opening angle correlation in the region from
 932 about 165° to 180° , which can be seen in Figs. 13 and
 933 27, as well as in Figs. 22 and 23. The effect is particularly
 934 strong for the neutron energy cuts being applied in the
 935 upper right plots of both Figs. 22 and 23. A comparison
 936 of the observed decrease after 160 degrees with the null
 937 hypothesis that the true distribution remains constant af-
 938 ter 160 degrees yields a p-value of 0.01. This indicates a
 939 1% probability of obtaining data as compatible with the
 940 above hypothesis as the data we observed. This is a fea-
 941 ture which does not seem to universally appear in either

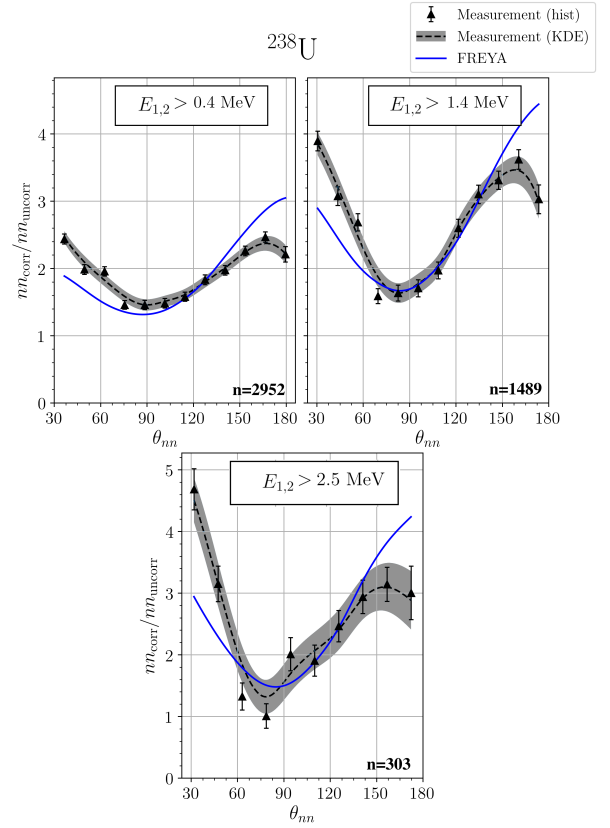


FIG. 22: θ_{nn} distribution with minimum energy threshold cuts applied. The number of events contributing to each plot, n , is shown. Note that the bottom plots of this figure and Fig. 23 are identical.

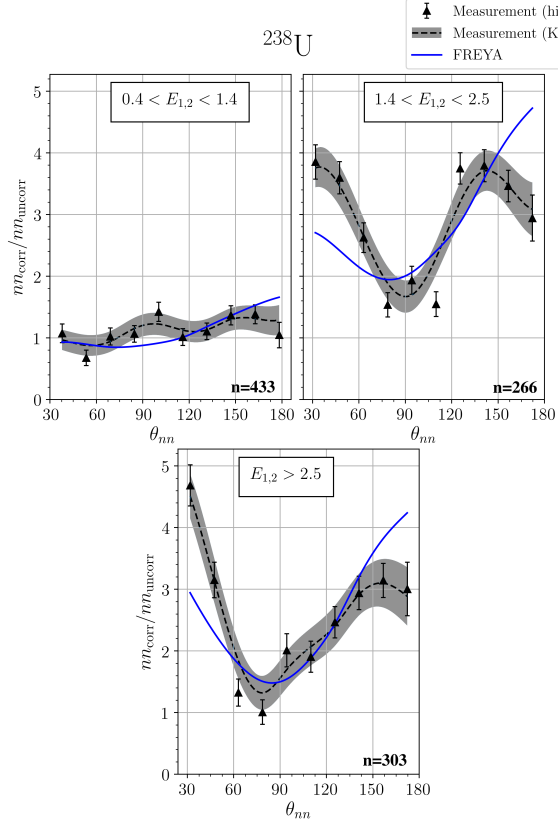


FIG. 23: θ_{nn} distribution with cuts requiring that the energy of both coincident neutrons be within the specified range. The number of events contributing to each plot, n , is shown. Note that the bottom plots of this figure and Fig. 22 are identical.

neutron-induced or spontaneous fission. A similar but less pronounced effect appears in the results reported in Ref. [11] for the thermal neutron-induced fission of ^{233}U and ^{235}U , but not for the spontaneous fission of ^{252}Cf or the neutron-induced fission of ^{239}Pu . The prominence of this effect observed in the present work may be a characteristic feature of the photofission of the even-even ^{238}U nucleus.

As previously discussed in section IC, photofission differs from spontaneous and neutron induced fission in that the fission fragments for the photon-induced reaction exhibit an asymmetry in their angle of emission, with the most likely orientation of the fission axis lying perpendicular to the direction of the incident photon. With this in mind, the following series of angular cuts were made on the data. Figure 26 shows the distributions of absolute opening angles of the n-n events for three different cuts on the value of the n-n opening angle. For n-n opening angles between 120° and 160° , there is an increased preponderance of both neutrons being emitted around 90° , consistent with the interpretation of kinematic focusing of neutrons coming from fission fragments which are themselves being emitted preferentially at 90° . However, in the opening angle region where the n-n correla-

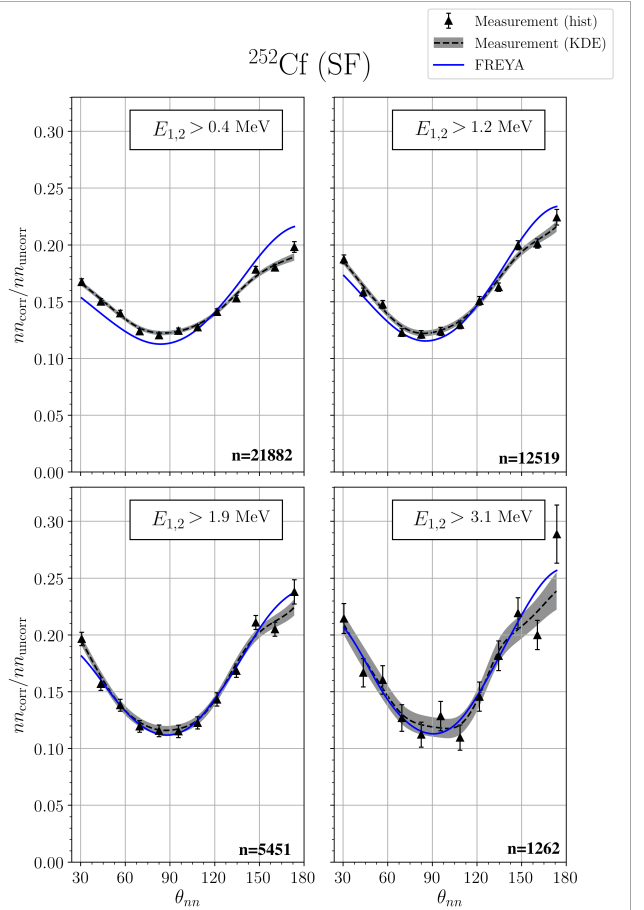


FIG. 24: θ_{nn} distribution a minimum energy threshold cuts applied. The number of events contributing to each plot, n , is shown. Note that the lower right plots of this figure and Fig. 25 are identical.

tion is reduced, from about 160° to 180° , this feature is less prominent.

Furthermore, if one plots the opening angle distributions for the case in which at least one neutron is emitted perpendicular to the incident photon versus the case in which neither neutron is emitted perpendicular to the incident photon (Fig. 27), one sees distinct differences. The fact that there are overall differences is not surprising, because in one case (Fig. 27 solid line) at least one neutron preferentially receives a kinematic boost from a fission fragment and in the other case (Fig. 27 dotted line) neither neutron does. However, the fact that the n-n correlation is reduced at 180° in opening angle when at least one of the neutrons is emitted along the preferred fission axis is unexpected. This is a feature which does not seem to appear in most previous measurements of either neutron-induced or spontaneous fission, as well as our present measurement on spontaneous fission. The attribution of this effect to the geometric coverage of the neutron detection system or to neutron elastic scatter-

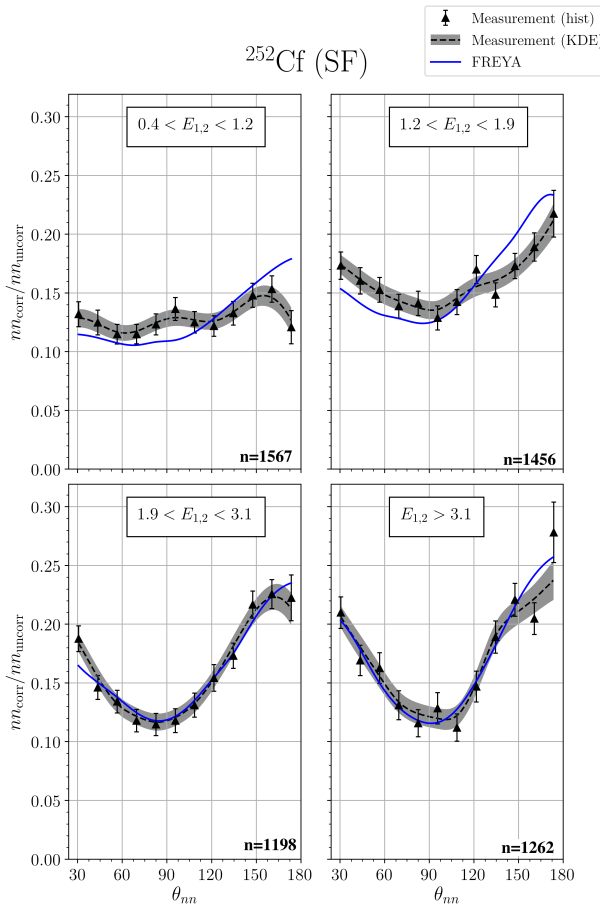


FIG. 25: θ_{nn} distribution with cuts requiring that the energy of both coincident neutrons be within the specified range. The number of events contributing to each plot, n , is shown. Note that the lower right plots of this figure and Fig. 24 are identical.

ing within the target was ruled out using simulations, as discussed in section V C.

These data are consistent with two possible explanations relating to the unique feature of the asymmetric angular emission of fission fragments in photofission. First, the neutrons may indeed be emitted isotropically in the rest frame of the fission fragment, but one fragment essentially shadows the neutrons emitted from the other fragment, either through absorption or scattering. Second, that there is, due to unknown reasons, a decrease in neutron emission along the fission axis. If it is the former case, then this effect has the potential to shed light on the time dependence of neutron emission, since shadowing would likely depend on the fission fragment separation. A definitive interpretation of this decreased n-n correlation for large opening angles in photo-fission requires further study.

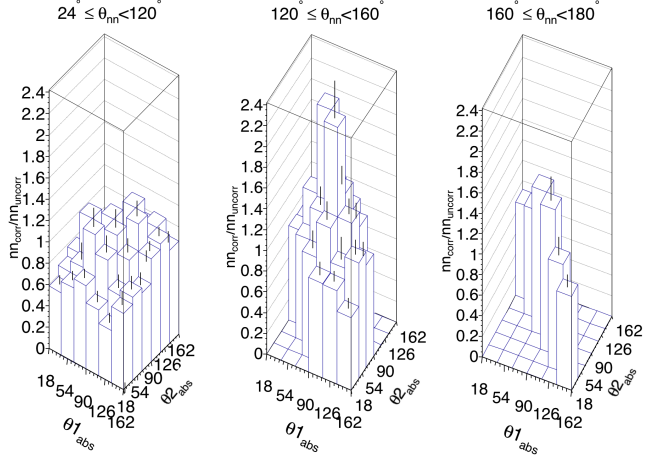


FIG. 26: Visualization of the correlation between the angles of each neutron with respect to the incident photon beam, denoted by $\theta_{1\text{abs}}$ and $\theta_{2\text{abs}}$. Empty bins exist because of intrinsic geometrical phase-space. Data taken from measurements of ^{238}U photofission.

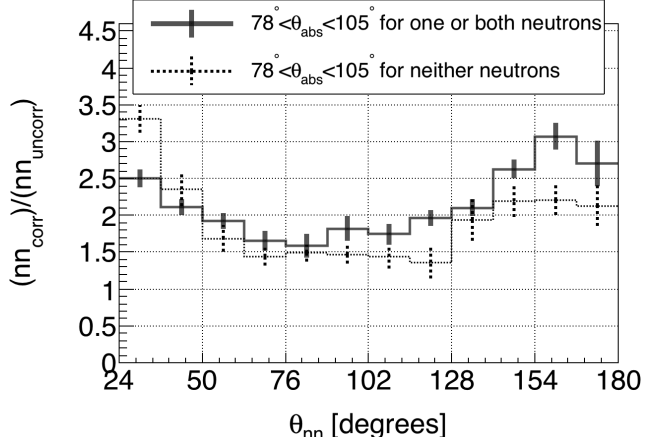


FIG. 27: Requiring that at least one of the coincident neutrons be emitted nearly perpendicular to the photon beam (solid line) produces an opening angle distribution that is different from that produced when it is required that both neutrons are emitted nearly parallel to the photon beam (dotted line). Data taken from measurements of ^{238}U photofission.

VII. CONCLUDING REMARKS

Neutron-neutron angular correlations in the photofission of ^{238}U were measured using 10.5 MeV end-point bremsstrahlung photons produced via a low duty factor, pulsed linear electron accelerator. The measured angular correlations reflect the underlying back-to-back nature of the fission fragments. The method of analysis used a single set of experimental data to produce an opening angle distribution of correlated and uncorrelated neutron pairs. A ratio is taken between these two sets to provide a self-contained result of angular correlations, in that

the result is independent of neutron detector efficiencies. Neutron-neutron angular correlation measurements were also made using neutrons from the spontaneous fission of ^{252}Cf and show good agreement with previous measurements.

Measured n-n opening angle distributions from the photofission of ^{238}U are in great disagreement with the ad hoc photofission model included in FREYA version 2.0.3.

This is expected, because the model is only a crude approximation which uses a neutron-induced model to approximate photofission. The present measurement will be useful for fine-tuning photofission models included in future releases of FREYA.

In addition, we report for the first time a pronounced anomaly in the n-n angular distributions from photofission, in which the rate of neutron emission at opening angles near 180° is diminished, resulting in a local maximum at about 160° instead of the expected 180° . We offer two possible explanations for this effect. First, the neutrons may indeed be emitted isotropically in the rest frame of the fission fragment, but one fragment essentially shadows the neutrons emitted from the other fragment.

that there is, due to unknown reasons, a decrease in neutron emission along the fission axis. While these measurements do not provide a definitive interpretation of this decreased n-n correlation for large opening angles in photofission, further study may have the potential to shed light on the time evolution of neutron emission in photofission.

These first measurements of n-n correlations in photofission may provide the impetus for future modeling of the fundamental physics of fission.

VIII. ACKNOWLEDGMENTS

- This work has been supported by the National Nuclear Security Administration, grant DE-NA002488. We wish to thank the staff of the Idaho Accelerator Center for their assistance in this work. We also wish to acknowledge early contributions to this work by our friend and colleague the late David V. Jordan of the Pacific Northwest National Laboratory.
-
- [1] J. T. Caldwell, E. J. Dowdy, R. A. Alvarez, B. L. Berman, and P. Meyer. Experimental determination of photofission neutron multiplicities for ^{235}U , ^{236}U , ^{238}U , and ^{232}Th using monoenergetic photons. *Nuclear Science and Engineering*, 73(2):153–163, 1980.
- [2] G. A. Petrov. Current status of the search for scission neutrons in fission and estimation of their main characteristics. *AIP Conference Proceedings*, 798(1):205–212, 2005.
- [3] Harry R. Bowman, Stanley G. Thompson, J. C. D. Milton, and Wladyslaw J. Swiatecki. Velocity and angular distributions of prompt neutrons from spontaneous fission of Cf^{252} . *Phys. Rev.*, 126:2120–2136, Jun 1962.
- [4] C. Budtz-Jørgensen and H.-H. Knitter. Simultaneous investigation of fission fragments and neutrons in ^{252}Cf (SF). *Nuclear Physics A*, 490(2):307 – 328, 1988.
- [5] P. Talou, R. Vogt, J. Randrup, M. E. Rising, S. A. Pozzi, J. Verbeke, M. T. Andrews, S. D. Clarke, P. Jaffke, M. Jandel, T. Kawano, M. J. Marcath, K. Meierbachtol, L. Nakae, G. Rusev, A. Sood, I. Stetcu, and C. Walker. Correlated prompt fission data in transport simulations. *The European Physical Journal A*, 54(1):9, Jan 2018.
- [6] S. Debenedetti, J. E. Francis, W. M. Preston, and T. W. Bonner. Angular dependence of coincidences between fission neutrons. *Phys. Rev.*, 74:1645–1650, Dec 1948.
- [7] J. S. Pringle and F. D. Brooks. Angular correlation of neutrons from spontaneous fission of ^{252}Cf . *Phys. Rev. Lett.*, 35:1563–1566, Dec 1975.
- [8] J. M. Verbeke, L. F. Nakae, and R. Vogt. Neutron-neutron angular correlations in spontaneous fission of ^{252}Cf and ^{240}Pu . *Phys. Rev. C*, 97:044601, Apr 2018.
- [9] Sara A. Pozzi, Brian Wieger, Andreas Enqvist, Shaun D. Clarke, Marek Flaska, Matthew Marcath, Edward Larsen, Robert C. Haight, and Enrico Padovani. Correlated neutron emissions from ^{252}Cf . *Nuclear Science and Engineering*, 178(2):250–260, 2014.
- [10] A. M. Gagarski, I. S. Guseva, V. E. Sokolov, G. V. Val'ski, G. A. Petrov, D. O. Krinitin, D. V. Nikolaev, T. A. Zavarukhina, and V. I. Petrova. Neutron-neutron angular correlations in spontaneous fission of ^{252}Cf . *Bulletin of the Russian Academy of Sciences, Physics*, 72:773–777, July 2008.
- [11] V. E. Sokolov and G. A. Petrov. Investigation of the angular dependences of neutron-neutron coincidences from ^{252}Cf , ^{235}U , ^{233}U and ^{239}Pu fission in search of scission neutrons. *Proc. XVIII Internat. Seminar on Interaction of Neutrons with Nuclei (ISSIN-18)*, pages 108–118, 2010.
- [12] Matthew J. Marcath, Tony H. Shin, Shaun D. Clarke, Paolo Peerani, and Sara A. Pozzi. Neutron angular distribution in plutonium-240 spontaneous fission. *Nuclear Instruments and Methods in Physics Research, Section A: Accelerators, Spectrometers, Detectors and Associated Equipment*, 830:163–169, 9 2016.
- [13] S Nair, D B Gayther, B H Patrick, and E M Bowey. Fission-neutron and fragment angular distributions from threshold photofission of ^{232}Th and ^{238}U . *Journal of Physics G: Nuclear Physics*, 3(7):965, 1977.
- [14] Jefferson Lab. CODA 2.6, 2015.
- [15] Sara A Pozzi, Enrico Padovani, and Marzio Marseguerra. MCNP-PoliMi: a Monte-Carlo code for correlation measurements. *Nuclear Instruments and Methods in Physics Research Section A: Accelerators, Spectrometers, Detectors and Associated Equipment*, 513(3):550 – 558, 2003.
- [16] Eric C. Miller, Shaun D. Clarke, Marek Flaska, Sara A. Pozzi, and Enrico Padovani. MCNPX-PoliMi post-processing algorithm for detector response simulations. *JNMM, Journal of the Institute of Nuclear Materials Management*, 40(2):34–41, 12 2012.

- 1123 [17] Lawrence Berkeley National LaboratoryLawrence Liver- 1132
1124 more National LaboratoryLos Almost National Labora- 1133
1125 toryUniversity of Michigan Nuclear Engineering. *FREYA* 1134
1126 *2.0.3*, 2016. 1135
- 1127 [18] S. D. Clarke, B. M. Wieger, A. Enqvist, R. Vogt, J. Ran- 1136
1128 drup, R. C. Haight, H. Y. Lee, B. A. Perdue, E. Kwan, 1137
1129 C. Y. Wu, R. A. Henderson, and S. A. Pozzi. Mea- 1138
1130 surement of the energy and multiplicity distributions of 1139
1131 neutrons from the photofission of ^{235}U . *Phys. Rev. C*, 1140
95:064612, Jun 2017.
- 1132 [19] Krishichayan, M. Bhike, A. P. Tonchev, and W. Tornow.
Fission product yield measurements using monoenergetic
photon beams. In *European Physical Journal Web of
Conferences*, volume 146 of *European Physical Journal
Web of Conferences*, page 04018, September 2017.
- 1133 [20] Kyle Cranmer. Kernel estimation in high-energy physics.
Computer Physics Communications, 136(3):198–207,
2001.